Co-sputtering of gold and copper onto liquids: a route towards the production of porous gold nanoparticles

Adrien Chauvin[1*], Anastasiya Sergievskaya[2], Abdel-Aziz El Mel[3], Anna Fucikova[4], Cinthia Antunes Corrêa[1,5], Elen Duverger-Nédellec[1], David Cornil[6], Jérôme Cornil[6], Pierre-Yves Tessier[3], Milan Dopita[1] and Stephanos Konstantinidis[2]

[1] Department of Condensed Matter Physics, Faculty of Mathematics and Physics, Charles University, Ke Karlovu 5, 121 16 Prahanong 2, Czech Republic.
[2] Chimie des Interactions Plasma-Surface (ChIPS), CIRMAP, Research Institute for Materials Science and Engineering, University of Mons, 23 Place du Parc, B-7000 Mons, Belgium.
[3] Université de Nantes, CNRS, Institut des Matériaux Jean Rouxel, IMN, 2 rue de la Houssinière, 44000, Nantes, France.
[4] Department of Chemical Physics and Optics, Faculty of Mathematics and Physics, Charles University, Ke Karlovu 5, 121 16 Praha 2, Czech Republic.
[5] Institute of Physics of the Czech Academy of Sciences, Cukrovarnická 10/112, 162 00 Prague 6, Czech Republic.
[6] Laboratory for Chemistry of Novel Materials (CMN), University of Mons, Place du Parc 20, Mons 7000, Belgium.

E-mail: andrien.chauvin@karlov.mff.cuni.cz

Received xxxxxx
Accepted for publication xxxxxx
Published xxxxxx

Abstract

Effective methods for the synthesis of high-purity nanoparticles (NPs) have been extensively studied for a few decades. Among others, cold plasma-based sputtering metals onto a liquid substrate appears to be a very promising technique for the synthesis of high-purity NPs. The process enables the production of very small NPs without using any toxic reagents and complex chemical synthesis routes, and enables the synthesis of alloy NPs which can be the first step towards the formation of porous NPs. In this paper, the synthesis of gold-copper alloy NPs has been performed by co-sputtering gold and copper targets over pentaerythritol ethoxylate (PEEL). The resulting solutions contain a mixture of gold, copper oxide, and alloy NPs having a radius of few angstroms. The annealing of these NPs, inside the solution, has been performed in order to increase their size and further induce the dealloying of the Au-Cu NPs. The resulting NPs exhibit either a nanoporous structure or are self-organized in an agglomerate of small NPs.

Keywords: nanoparticles, porous, magnetron co-sputtering, alloy, liquid substrate, sputtering onto liquids, dealloying

 © xxxx IOP Publishing Ltd

1. Introduction

Metal nanoparticles (NPs) have been widely investigated due to their impressive properties which make them highly promising for a large range of applications [1]. Their peculiar properties originate from the large surface-to-volume ratio and quantum confinement effects [2]. Besides the abundant research on NPs, the development of hollow and nanoporous NPs attracts great attention for catalysis or biomedical applications [3–5]. For example, it has been revealed that hollow NPs are more efficient for heat generation than solid NPs when exposed to near-infrared radiation, which makes them attractive for cancer treatment applications [6,7]. Currently, the synthesis of porous or hollow nanostructures is mostly based on the Kirkendall effect [8,9], and the galvanic replacement reactions [10]. The galvanic replacement methods often leads to the formation of polycrystalline microstructures which exhibit a high density of defects [11]. On the other hand, the Kirkendall effect requires high temperatures to induce the required bulk interdiffusion, which results in the transformation of a hollow nanostructure into a solid one [12]. To overcome those drawbacks, the dealloying process appears to be a suitable alternative [13]. Dealloying, or selective leaching, is based on the removal of a less noble metal from an alloy to create a crystalline and stable nanoporous structure [14–16]. This method has been successfully used for the production of porous NPs [13,17,18]. The reported approaches deals with the creation of alloy NPs either combined with the substrate [17], or by using a chemical procedure [18]. However, the development of dealloying in practical applications is linked to the ability of dispersing the porous NPs in a non-toxic liquid media. In general, there are two different ways to synthesize NPs, i.e., the chemical and physical procedures [2]. On one hand, typical preparation of metal NPs by the chemical way involves the chemical reduction of metal ions into NPs in solution with a reducing agent [19]. This method has been extensively developed due to its high versatility in terms of controlling the NPs sizes. However, due to the complicated, costly, and energy-consuming procedures involved in the purification and separation of by-products, NPs preparations that avoid such contaminations are highly valued. On the other hand, the physical way involves the transformation of bulk material into NPs. This can be done by photon, or ion irradiation, heating, or mechanical milling of the source material [2]. Among all NP preparation routes, the method involving the deposition of atoms over liquid matrices has recently attracted considerable attention [2]. This method is very promising due to the high purity of the obtained NPs. The nanoparticle-forming atoms are emitted from the surface of the source material by bombarding ions extracted from a plasma, i.e. a technique named sputtering. Sputtering is a vacuum-based process, therefore low vapor pressure liquid matrices must withstand high vacuum ($\leq 10^{-3}$ Pa) [20]. Liquids such as pentaerythritol ethoxylate (PEEL) or polyethylene glycol (PEG) meet this requirement. Moreover, they are cheap, ecologically friendly, and biocompatible [2,21,22]. The coalescence mechanisms taking place during the formation of the NPs is not yet fully understood but it has been reported that the metallic NPs coalesce on the surface of the liquid matrix [23,24], then the growth may further proceeds and the NPs form inside the liquid [23,25]. More recently, it was reported that the oxidation during venting may play a role on NPs formation [21]. Beyond the synthesis of homogeneous metal NPs, alloy NPs can also be successfully synthesized by this approach [26,27]. Most of the publications on bimetallic alloy NPs formed via sputtering onto a liquid substrate mainly rely on the sputtering of a monometallic target combined with chemical reduction [28], the sputtering of an alloy target [29,30] or by sequential sputtering [31]. However, the newly created NPs exhibit mostly core-shell structure and the set-up requires fabricating different targets in order to vary the composition of NPs. An interesting alternative is the co-sputtering of two metallic targets to get alloy NPs hence allowing to easily tune their compositions by varying the electric power applied on each cathode [32–35]. In the present article, we discuss the preparation of gold-copper alloy NPs by co-sputtering onto a liquid substrate and the subsequent creation of nanoporous NPs by further dealloying. For the first time the co-sputtering of gold and copper targets was done onto PEEL liquid substrate. The subsequent dealloying of the alloy NPs allowed fabricating nanoporous gold NPs and close-packed NPs structures.

2. Methods

2.1 Synthesis of NPs

The pentaerythritol ethoxylate (PEEL) was purchased from Sigma Aldrich and stored without any particular precaution. The NPs were synthesized by DC co-sputtering, in pure argon plasma, of Au (diameter: 76.2 mm; purity: 99.99%) and Cu (diameter: 76.2 mm; purity: 99.99%) targets in confocal geometry. For these sputtering experiments, 2.5 ml of PEEL was poured into a watch glass supported by a homemade metal holder (80 mm of diameter) located 130 mm from the magnetron sources; the angle between each magnetron source axis and the normal to the sample holder was 30°. The electrical power applied to the Cu target was fixed to 75 W (with a sputtering current of 175 mA) for a deposition rate of 15 nm/min whereas the one applied to the Au target was varied in between 17, 12 and 8 W (with a sputtering current of 49, 38 and 26 mA, respectively) in order to vary the deposition rate from 5.1, 3.6, and 2.4 nm/min, respectively, and modify the average composition from 26, 23 to 11 at.% of Au, respectively [36]. These powers have been selected in order to avoid the creation of a film on the surface of the PEEL as observed for higher power conditions [37], while still

Table 1. Deposition conditions used in this study

Name	Sample 1	Sample 2	Sample 3	Sample 4	Sample 5
Power applied on gold target (W)	17	17	12	8	-
Power applied on copper target (W)	-	75	75	75	75
Amount of sputtered material inside the liquid (mg/cm3)	2.2	5.3	4.6	4.1	3

producing substantial amounts of NPs. The average content of the less noble metal, i.e. copper, within the alloy was selected in order to be higher than the parting The parting limit is defined as the concentration threshold below which the dissolution of the less noble component from a homogeneous binary alloy occurs [16]. All depositions were carried out at a pressure of 0.5 Pa without applying any intentional heating to the substrate. For all depositions, the base pressure was less than 5×10^{-5} Pa and the rotation speed of the substrate was fixed to 5 rpm to minimize the variation in deposition flux and subsequently the spatial distribution of gold and copper atoms over the surface of the liquid. The deposition time was fixed to 5 min. Deposition conditions, denotations and estimations of the amount of sputtered materials inside each solution are summarized in Table 1.

2.2 Annealing of the NPs

A glycerol bath was kept to the desired temperature using a hot plate. Magnetic stirring was induced at 100 rpm to homogenize the temperature of the oil bath. Then, a glass vessel with the PEEL solution containing the NPs was suspended in this bath. The annealing was performed in air atmosphere. In order to achieve a complete coalescence of the NPs, the annealing time was fixed to 5 h. Three annealing temperatures (80, 150, and 200 °C) were selected to tune the size of the NPs.

2.3 Preparation of the TEM grids

The TEM grids were prepared by dipping a gold grid with holey carbon coating or nickel grid with lacey carbon coating in the PEEL solution containing the NPs. The grid was heated up to 50 °C on a hot plate during 30 min over an aluminium foil in air atmosphere. Then, 10 µl of ethanol was dropped on the grid and dried for 10 min. This step was repeated 3 times. Finally, the grid was dipped into ethanol for 1 h, transferred into clean ethanol and left for 1 h. This procedure leads to the removal of excessive liquid PEEL, whereas the NPs were bound to the grid. The resulting grid was then stored in vacuum for further processing.

2.4 Dealloying of the NPs

The NPs were dealloyed by dipping a gold grid containing the NPs into concentrated nitric acid (65 %) for 1 min. At the end of the treatment time, the grid was immersed in deionized water for several minutes to stop the chemical etching and to remove the residue of nitric acid.

2.5 Characterization

For UV-visible spectroscopy (UV-Vis), the PEEL solutions containing NPs were diluted in ethanol (1/50), poured into a 1 cm plastic cuvette and analysed using a Perkin Elmer LAMBDA 650 equipment. The spectra were recorded between 300 and 900 nm at room temperature. Pure ethanol was taken as a reference. The morphology of the particles was monitored using a JEOL 2200 FS transmission electron microscope (TEM) with an acceleration voltage of 200 kV. For small-angle X-ray scattering (SAXS) analysis, the PEEL liquid containing the NPs was poured into a borosilicate capillary having an outer diameter of 1 mm and a wall thickness of 0.01 mm, as provided by WJM-Glas Müller GmbH. The SAXS measurements were performed using a Xeuss 2.0 (Xenocs) equipped with a Cu microfocus X-ray source (wavelength $\lambda = 0.15418$ nm). The sample to detector distance was tuned between 350 to 2500 mm to reach the q range of 0.25 - 149.5 $Å^{-1}$ in a high-resolution mode (beam size 0.6×0.6 mm^2). SAXS patterns measured in transmission mode were acquired with a Pilatus 200 k (Dectris) hybrid pixel single-photon counting detector. Measured data were azimuthally integrated using Foxtrot software[38] and corrected for background scattering from capillary and PEEL liquid.

2.6 DFT calculations

Density Functional Theory (DFT)-based total energy calculations were performed in order to better understand the chemical interactions between the liquid PEEL and the different NPs obtained in the sputtering experiments. DFT calculations were carried out with periodic boundary conditions, as implemented in the SIESTA 4.1 code [39]. As a first approximation the surface of the nanoparticles are modelled as flat surface. The exchange−correlation functional is described within the general gradient approximation using the Perdew−Burke−Ersenoff (PBE) functional [40]. A double-ζ polarized numerical atomic basis set is adopted for the valence electrons, whereas core electrons are described with Troullier−Martin pseudopotentials [41]. A mesh cutoff of 250 Ry and a Monkhorst−Pack grid of ($2 \times 2 \times 1$) k-points were used during the relaxation of the interface (PEEL molecule together with the top two surface layers). These parameters

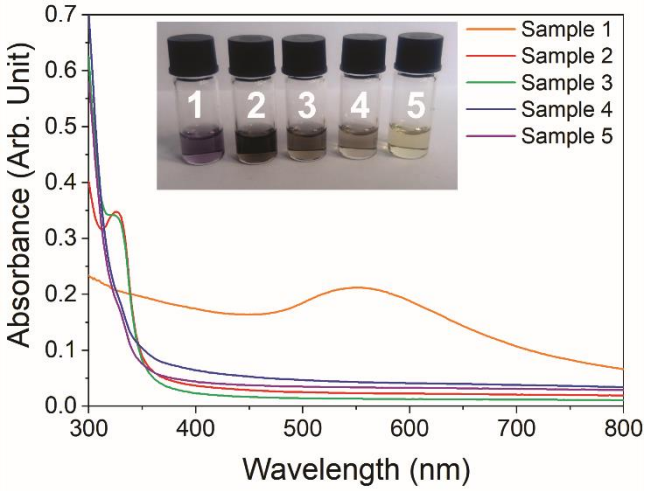

Figure 1. Absorbance spectra of diluted PEEL solution with Au NPs (sample 1 - orange), Cu NPs (sample 5 - purple), and Au-Cu alloy NPs produced by co-sputtering with a power of 8 (sample 4 - blue), 12 (sample 3 - green) and 17 W (sample 2 - red) at the Au target and 75 W at the Cu target. The inset corresponds to the PEEL solution containing the NPs diluted in ethanol from sample 1 to sample 5 (left to right).

were increased to 400 Ry and (4 × 4 × 1) for estimating the interaction energy. For the sake of computational facility, a simplified version of the PEEL molecule was used by shortening the aliphatic chains to end up with the pentaerythriol molecule $C(CH_2OH)_4$. This model molecule was first fully relaxed in the isolated state using a large unit cell of (30 x 30 × 30) $Å^3$ to avoid intermolecular interactions. We then studied the interactions of this model molecule with several surfaces, representing metal-based NPs made of gold, gold/copper and pure and oxidized copper, by considering the stable crystalline Au (111), Au_3Cu (111), AuCu (111), $AuCu_3$ (111), Cu (111) and Cu_2O (111) surfaces respectively; details about the model surfaces are provided in Supporting Information 1. For each surface, two initial conformations were considered to model a monodentate or a bidentate interaction of the PEEL molecule by approaching the neutral molecule with one or two hydroxyl groups oriented toward the surface. The geometry relaxation was performed using the conjugated gradient formalism with a 0.04 $eVÅ^{-1}$ convergence criterion on the atomic forces. Only the molecule and the top two layers over the five were allowed to relax. The interaction energy was calculated on the final relaxed geometry using the expression:

$$E_{int}=E_{surf/PEEL} - [E_{PEEL}+E_{surf}]$$

where $E_{surf/PEEL}$ is the total energy of the full interface in its optimized geometry and E_{PEEL} and E_{surf} are the energy of the free molecule and the bare surface in their interface geometry, respectively. This approach was previously used to investigate the interaction of PEEL molecule on titanium and silver oxide surfaces [21].

3 RESULTS AND DISCUSSION

3.1 UV-Vis spectrophotometry of the sputtered NPs

The NPs are obtained by sputtering either the gold or copper target separately, or by sputtering simultaneously these two targets over the PEEL liquid. Before the UV-Vis spectrophotometry analysis, a naked eyes observation of the solution was performed. The inset of the Figure 1 corresponds to solution diluted in ethanol. It is important to stress here that the dilution in ethanol didn't modify the colour of the solution. Depending on the working parameters, solutions with different colours are obtained, hence demonstrating the presence of NPs. Indeed, the pure PEEL liquid is transparent. When only using the gold target (sample 1), the resulting solution has a purple colour, as already reported in the literature [23]. The solution made by sputtering only the copper target (sample 5) is brown right after the sputtering but the solution turns yellow after a few days of storage. The change in colour is linked to the oxidation of the copper NPs [42]. Finally, solutions obtained by co-sputtering both the gold and copper targets (sample 2, 3 and 4) are black without any aggregation or flocculation. All samples, except those containing only Au NPs (sample 1), show high stability in time without sedimentation. The high dispersion and stability of the NPs inside the liquid are linked to the nature of the oil (i.e. PEEL) and the sputtered materials. This point will be discussed later in this paper. Moreover, due to the multiple hydroxyl groups of the PEEL, the coordination ability of the liquid interface is high. So, the diffusion of the sputtered atoms arriving onto the surface is limited. This leads to dispersed NPs onto the gas/liquid interface and ultimately, inside the liquid [2,43]. Figure 1 presents the UV-vis absorption spectra of the dispersed NPs in ethanol. For sample 1, the UV-vis spectrum shows a surface plasmon resonance (SPR) with a maximum located at around 540 nm. It has been confirmed previously that a clear SPR is observed only for Au NPs larger than 20 Å [44]. The shift of the maximum of the SPR band representative of gold and located at 520 nm is due to the aggregation of Au particles, as already reported for metals sputtered onto liquids [45]. Moreover, a redshift of the SPR band might also indicate the increase of the size of the initial gold NPs [46]. This observation gives us a first indication about the Au NPs size. For sample 5, prepared by sputtering only copper, no SPR corresponding to the presence of copper NP is observed. SPR of copper should appear at 580 nm, as reported in the literature [33]. This behaviour may be due to the formation of very small NPs (< 20 Å) [47,48]. The oxidation of the copper NPs can also induce the disappearance of the SPR signal typical of pure copper NPs [42]. Indeed, it was stressed before that the colour of the solution is yellow

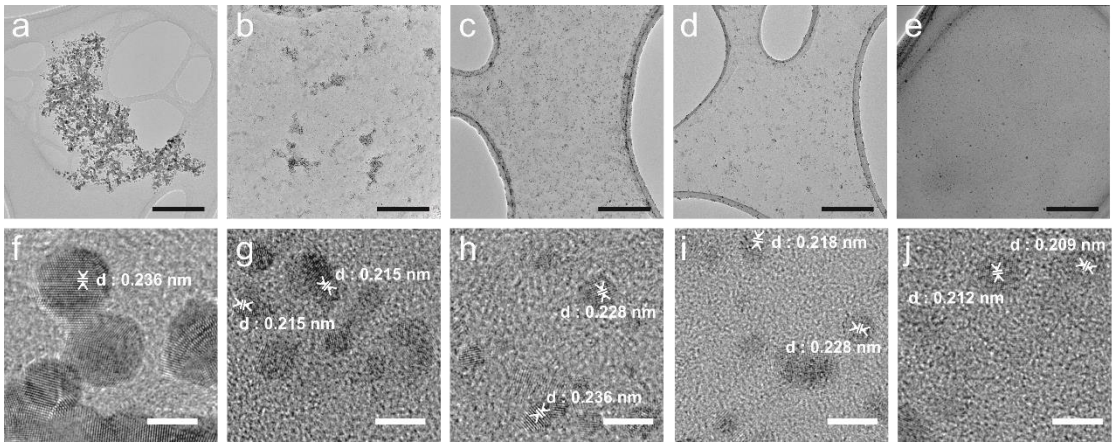

Figure 2. TEM micrograph at (a-e) low and (f-j) high magnification of Au NPs (sample 1 - a and f), Cu NPs (sample 5 - e and j), and Au-Cu alloy NPs obtained by co-sputtering with a power at the Cu target of 75 W and 8 (sample 4 - d and i), 12 (sample 3 - c and h) and 17 W (sample 2 - b and g) at the Au target. (f-j) High-resolution TEM images display the lattice fringes of some nanoparticles. Black scale bar: 200 nm, white scale bar: 5 nm.

which is consistent with the colour of copper oxide NPs in solution. For samples 2-4, no SPR peak corresponding either to copper, gold or alloy NPs is observed. This can be explained by the low concentration of gold NPs and the large amounts of copper oxide NPs. Moreover, the formation of small Au-Cu alloy NPs can hinder the appearance of a well-defined characteristic SPR peak [33]. On the other hand, a shoulder is observed in the UV-vis spectra around 320 nm and 350 nm for samples produced when the copper target is used (sample 2-5). The shoulder is more pronounced when increasing the total sputter power on both targets. This behaviour is explained by the higher amount of material deposited onto the liquid surface as the sputter power is increased [21]. This shoulder around 350 nm was already reported in the literature for Cu_2O NPs [49,50]. It can be due to the direct forbidden band-gap induced by the change in the absorption of Cu_2O NPs depending on their diameters. Indeed, a shift of the band-gap is observed from 2.09 eV for bulk Cu_2O toward higher energy when the diameter of Cu_2O NPs decreases [51,52].

3.2 TEM of the sputtered NPs

A TEM observation of the NPs obtained after sputtering over PEEL is performed. In order to prepare the grid with NPs, a procedure has been developed to remove liquid PEEL from the samples. This process is described in detail in the experimental part. The resulting micrographs are displayed in Figure 2. At low magnification (Figure 2a-e), it can be seen that the process used to prepare the grids allows for a good dispersion along with a high quantity of NPs on the grid, whatever the sample probed. Moreover, only a low amount of PEEL residue has been detected over the whole grid. For sample 1, the Au NPs appear to be aggregated and interconnected creating a ligament structure (Figure 2a). This structure was already reported in the literature for the

Table 2. Calculated interaction energies, charge transferred and total effective bond order between the (OH- terminated) model PEEL molecules and different surfaces.

Nature of the surface	Binding mode	Adsorption energy (eV)	Charge on molecule (|e|)	Total EBO
Au	monodentate	-0.22	0.27	0.85
	bidentate	-0.27	0.26	0.80
Au_3Cu	monodentate	-0.22	0.20	0.84
	bidentate	-0.41	0.24	0.99
AuCu	monodentate	-0.37	0.23	0.87
	bidentate	-0.48	0.23	1.04
$AuCu_3$	monodentate	-0.36	0.24	0.90
	bidentate	-0.45	0.26	1.02
Cu	monodentate	-0.29	0.26	0.82
	bidentate	-0.40	0.25	1.04
Cu_2O	bidentate to 1 Cu atom	-1.71	0.24	1.40
	bidentate to 2 Cu atoms	-1.72	0.25	1.41

sputtering of gold over liquid [23]. Those ligaments can eventually arise from the fact that a film forms on the surface of the PEEL liquid during the sputter deposition experiment. In order to better analyse this thin film, the sputtering of the gold target was performed in the same condition, but for longer duration, i.e. 20 min instead of 5 min (Figure S1). The resulting thin film shows a nanoporous morphology throughout the whole film thickness. This nanoporous structure is constituted of interconnected ligament structures made of NPs. The formation of such thin film is linked to the viscosity [53] and the deposition rate [20], but is also due to the low affinity of gold surfaces for PEEL [43]. Indeed, for sample 5 made by sputtering only the copper target at a power higher than the one used for gold sputtering, and therefore with a larger deposition rate, no film was observed. Therefore, the affinity of the PEEL for the sputtered material is a key parameter for the formation of a thin film at the surface of the liquid. In order to quantify the affinity of the different surfaces for the PEEL molecule, quantum chemistry – based calculations, carried out at the DFT level, have been performed (Supplementary Information 1). The calculated interaction energies between a (simplified) PEEL molecules and the different surfaces are summarized in Table 2. The Table 2 also provides the charge transfer and the total effective bond order between the OH-terminated PEEL molecule and the difference surfaces modelled.

It can be noticed that the affinity between PEEL molecules, either with one or two chemical bonds (i.e. monodentate or bidentate configuration, respectively), and a gold surface is low and equals to -0.22 eV and -0.27 eV, respectively. This situation can be compared to that reached between PEEL and a copper surface (-0.29 eV and -0.40 eV) or a copper oxide surface (-1.71 eV and -1.72 eV). The preference for copper is consistent with the difference in electronegativity of the involved species ($\chi O = 3.44$; $\chi Au = 2.54$; $\chi Cu = 1.90$). Indeed, a systematic bonding of OH with copper atom is obtained after optimization of the PEEL/alloy interfaces. Our calculations also show that the charge transfer is very similar (see Table 2) for all compounds and does not explain the large difference between metals/metal alloys and Cu_2O. In contrast, the distinct behaviour of Cu_2O is explained by the bond order which is sensibly higher only for this system. This low affinity encountered for the PEEL-Au couple induces the creation of a thin film on the surface of the PEEL liquid, since the Au atoms and PEEL molecules seek to stay separated to minimize the energy of the system.

At higher magnification (Figure 2f), the TEM micrograph of Au NPs reveals a well-crystallized structure. However, when observing at low magnification (Figure 2b, c, and d) the samples 2-4, the ligament structure observed previously for the sample 1 made of gold is not observed anymore. In this case, the affinity of PEEL towards the gold-copper alloy surface appears to be sufficient (around -0.40 eV) to allow for a good dispersion of the NPs (Table 2). Moreover, we expect the PEEL molecules to fully stabilize the copper oxide and alloy NPs. Indeed, no sedimentation is observed and a stabilizing PEEL shell surrounding the NPs should form [21]. At high magnification, the alloy NPs (Figure 2g, h and i) turn out to be similar whatever the conditions, with an apparent diameter smaller than that of the Au NPs. The TEM micrographs also reveal crystallized NPs. Finally, sample 5 shows a good dispersion of the NPs, as it can be observed at low magnification (Figure 2e) similar to the other samples made by co-sputtering. Indeed, in our case, the copper NPs are oxidized, as highlighted by the color of the solution [42]. The high affinity between the Cu_2O surface and the PEEL molecule evidenced by the calculations prevents the creation of a film (Table 2). At high magnification (Figure 2j), NPs are barely visible because of the thickness of the carbon membrane [42]. Moreover, the low contrast makes the observation of the NPs more difficult. However, the structure of the NPs appears to be well crystallized too.

Thanks to the TEM micrographs, a first evaluation of the NPs size can be achieved. The mean radius of the NP present in sample 1 was evaluated manually by taking the diameter of each of the connected 'NP' because of the ligament observed. However, for the other samples, the particle size distributions have been elucidated with the help of ImageJ software, which measures the areas of the particles on the images [54,55]. For about 1 000 NPs in each case, the particle radius, R_{TEM}, has been calculated from the projected area, A, on the images as:

$$R_{TEM} = \sqrt{(A/\pi)}$$

Then, the particle radius has been defined as the radius of a sphere of an equivalent cross-sectional area on the images. The mean radius size for gold NPs obtained for sample 1 is 28 Å. For samples 2, 3 and 4, the mean radius size is around 9 Å. Finally, for sample 5, the mean radius is 18 Å. The sizes of the NPs obtained are similar to those reported in the literature [33,42,45]. With the high magnification TEM images of sample 1-4 (Figure 2g-i), one can find that the crystal structure of the NP is face-centered cubic (fcc), and the morphology delineates a truncated octahedron (Figure S2). Indeed, it is often reported that, whatever the composition of the Au-Cu nanoalloy is, the preferred shapes remain the dodecahedron, truncated octahedron, and icosahedron [56,57]. The

Table 3. Summary of the radii obtain by SAXS measurements (R_{SAXS}) as compared to those obtained by TEM analysis (R_{TEM}).

Name	Sample 1	Sample 2	Sample 3	Sample 4	Sample 5
R_{SAXS} (Å)	40 ± 30	15 ± 7	13 ± 7	15 ± 8	13 ± 8
R_{TEM} (Å)	28 ± 8	9 ± 3	9 ± 2	10 ± 2	18 ± 8

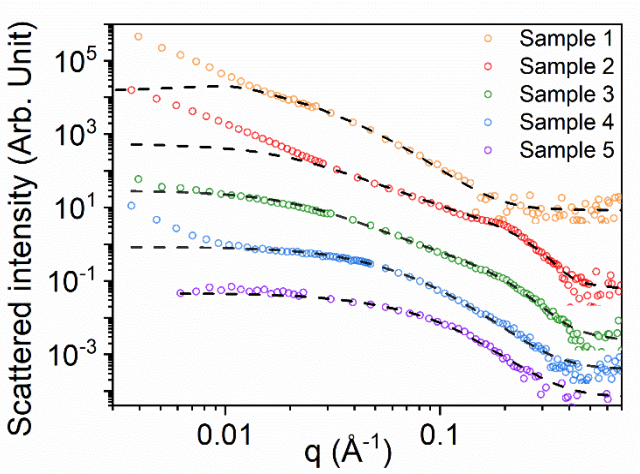

Figure 3. SAXS pattern (dot) and the resulting IRENA fit (dashed line) of Au NPs (sample 1 – orange), Cu NPs (sample 5 - violet), and Au-Cu alloy NPs produced using co-sputtering at a power of 75 W for Cu target and 8 (sample 4 - blue), 12 (sample 3 - green) and 17 W (sample 2 - red) for the Au target. The curves are shifted for better visualization.

crystalline structure of the NPs has been estimated. However, due to the small size and the dispersion of the NPs over the grids, the processing of electron diffraction patterns is difficult (Figure S3). Considering the TEM micrographs, the measurements of the lattice fringes showed different values depending on the nature of the NPs fabricated in each condition. Sample 1 exhibits a value of the lattice spacing of 2.36 Å, corresponding to the Au (111) fcc lattice parameters. On the other hand, sample 5 exhibits a lattice parameter of 2.09 Å, corresponding to the Cu (111) fcc lattice but also NPs with a lattice parameter equal to 2.12 Å, corresponding to the lattice parameter of cubic Cu_2O (200). Samples 2, 3, and 4 show a wide variety of lattice parameters. One can remark the presence of different lattice spacings between the lattice spacing of Cu (111) and Au (111) (Figure S4). This observation is the proof of the presence of gold-copper nanoalloys inside the samples made by co-sputtering both gold and copper targets. Moreover, it highlights the presence of an alloy solid solution rather than a phase separation. This statement has also been reported previously for the co-sputtering over other liquids [33,48].

3.3 SAXS analysis of the sputtered NPs

To confirm the mean radius value obtained by TEM, a SAXS investigation was performed. SAXS measurements were conducted on the PEEL solutions containing the NPs. The SAXS curves for the various sputtering conditions are shown in Figure 3. First, in the high q part (from 0.3 to 0.5 Å^{-1}) of the SAXS pattern, the slope of q^{-4} indicates that the particles are spherical and their surface is smooth [58]. The average radius and the dispersion of the NPs was evaluated by fitting the scattering data using a dedicated software, i.e. IGOR Pro implemented with IRENA package [59]. The fitting results are shown in Figure 3. In order to reduce the number of fitting parameters, as well as the range of available values necessary for the fitting procedure, approximations were made: i) the dispersion parameter and the shape of the NPs were estimated with the Guinier plot, ii) the radius value was fixed close to the radius obtained previously by TEM, and iii) the form factor was fixed to a spherical model according to the Porod law [60]. Moreover, in order to further improve the accuracy of the fitting of the scattering curves, it was crucial to use a hard sphere model as structure factor in most of the cases. The hard sphere model is one of the most widely used model for aggregated systems [61]. This structure factor is described by two parameters: the hard-sphere radius R_{HS} corresponding to the correlation distance of the particles within an aggregate and the mean hard-sphere volume η describing the degree of packing [62]. The spherical form factor was used to fit the scattering curves and the size distribution was fitted with a log-normal distribution, which is the most commonly used type of particle distribution [58,63]. The theoretical equations and the detailed parameters used for the fitting are shown in Supplementary Information 2. First, it can be noticed that the fitting curves show a significant deviation from the experimental pattern in the low q range (from 0.04 to 0.02 Å^{-1}). This discrepancy is linked to the presence of 'soft' agglomeration of NPs. This 'soft' agglomeration of NPs enhances the scattering in the low q region with random behaviour due to the weak bonding between NPs [64]. Then, due to the wide range of the NPs alloy composition (Figure S4), only a global fit of the curves has been performed. This global fit allows determining precisely the mean feature sizes of the NPs present inside the solutions. The SAXS pattern of gold NPs (Sample 1 - Figure 3) requires one component to provide a good fit. The value of the R_{HS} is 240 Å indicating the presence of large aggregates of NPs. The aggregation of NPs is also confirmed by the TEM image (Figure 2a). The resulting mean radius for the individual NP in sample 1, as reported by SAXS measurements, is 42 Å. The copper oxide NPs pattern (Sample 5 - Figure 3) is also fitted using only one component with a R_{HS} almost equals to the radius (~ 14 Å). This finding confirms that NPs are dispersed in the solution without interacting with each other. This observation is supported by the high affinity of the PEEL molecule for copper oxide NPs as revealed by the quantum chemistry-based calculations (Table 2). For samples synthetized by co-sputtering (samples 2, 3 and 4 in Figure 3), the model requires two components. This observation highlights the existence of two major populations of NPs in every sample made by co-sputtering. The first population of NPs has a mean radius of ~ 9 Å with a R_{HS} of ~ 15 Å. The second population is composed of larger NPs whose size ranges between 24 and 34 Å and is characterized by a R_{HS} ~

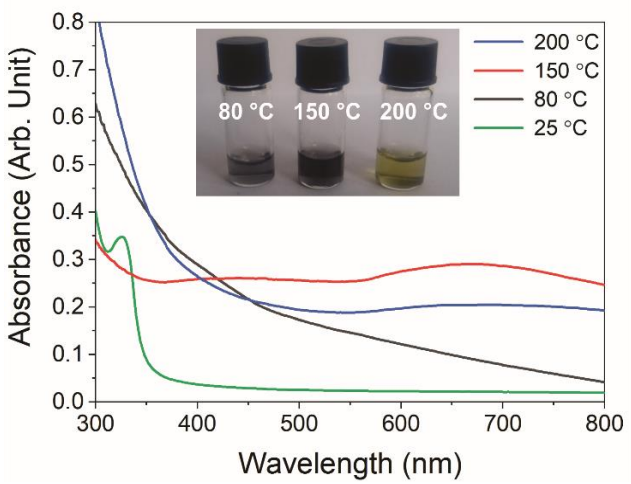

Figure 4. Absorbance spectra of a diluted PEEL solution containing Au-Cu alloy NPs (sample 2) after deposition and which are annealed at 80, 150 and 200 °C during 5 h. The inset corresponds to the visualization of annealed PEEL solutions containing the NPs annealed from 80 to 200 °C and diluted in ethanol (left to right).

40 Å. The small R_{HS} values, comparable to the radius of NPs, highlights the great dispersion of both NPs populations. As mentioned previously, the Au NPs tend to aggregate due to the low affinity of gold surface for PEEL molecules. So, in the case of samples synthesizes by co-sputtering, the presence of pure Au NPs population can be excluded. Nevertheless, the co-sputtered gold and copper induces the formation of Au-Cu alloy NPs. As described by the DFT calculations, the Au-Cu alloy surface has a higher affinity for PEEL than the gold surface (except for Au_3Cu) so that the creation of Au-Cu alloy NPs dispersed in PEEL can be expected. It is important to stress here that each sample made by co-sputtering exhibits a different SAXS pattern. This observation is linked to the different nature of each sample. From the curve fits, one can obtained the average size distribution of the particles inside each sample. The resulting mean radii are summarized in Table 3.

The here reported radii, as obtained from SAXS measurements, are in line with the values reported for copper oxide NPs and gold-copper alloy NPs [33]. However, the NPs made of gold are larger than those reported in the literature [33,65]. For most of the samples, a discrepancy is found when comparing the mean radii obtained by fitting the SAXS patterns with IRENA with those extracted from TEM observations. Considering the TEM images presented in Figure 2, one can notice that some particles are not spherical. The variation in the particle shape makes the analysis based on the assumption of spherical geometry less reliable and are probably the origin of the disagreement between SAXS and TEM data [66]. On the other hand, the process involving the preparation of the grids may also induce a selective removal of NPs, which is not the case when SAXS samples are prepared. Overall, the NP radius evaluated by SAXS is assumed to be more reliable because it is an integral method. According to this evaluation, the density of NPs inside the solution can be estimated at 3×10^{16} NPs/cm^3 for all sample 2 to 5 and 4×10^{14} NPs/cm^3 for sample 1.

After the characterization of the as deposited NPs, the PEEL solutions containing the NPs were heated up to increase their size. As reported previously for the dealloying of NPs, the diameters of the NPs has to be at least equal to 150 Å for dealloying to occur [18]. Moreover, as the size of the different NPs in solutions obtained by co-sputtering are similar for the three conditions and all of them contain Au-Cu alloy NPs, only sample 2 was studied due to the highest amount of material present in the solution. The temperature was

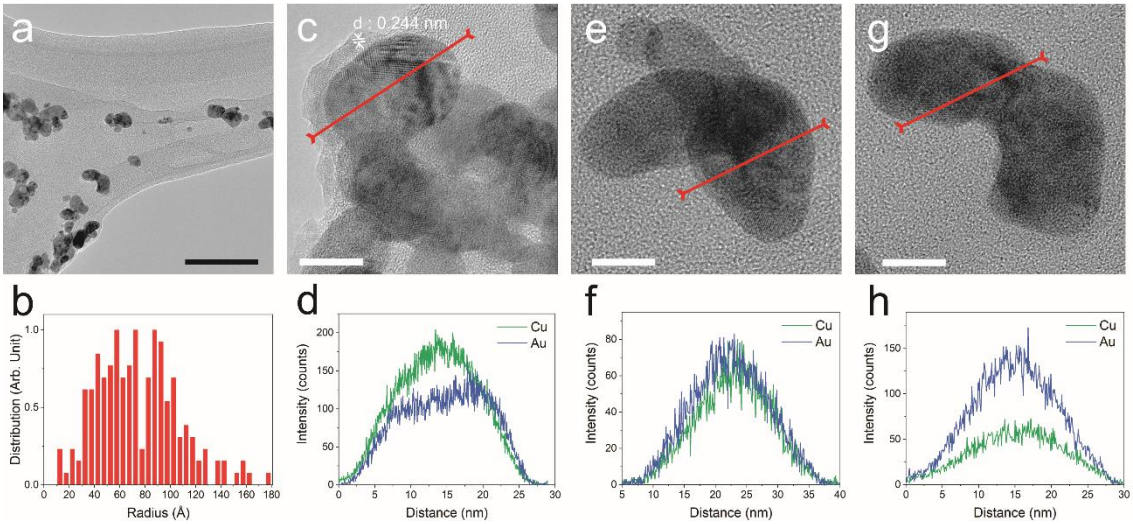

Figure 5. TEM micrograph of Au-Cu alloy NPs (sample 2) annealed at 200 °C during 5 h at (a) low magnification with (b) the resulting distribution of the NPs radii and (c, e and g) TEM micrographs at high magnification of selected Au-Cu NPs and (d, f, and h) the corresponding EDS line scan. Black scale bar: 100 nm, white scale bar: 10 nm.

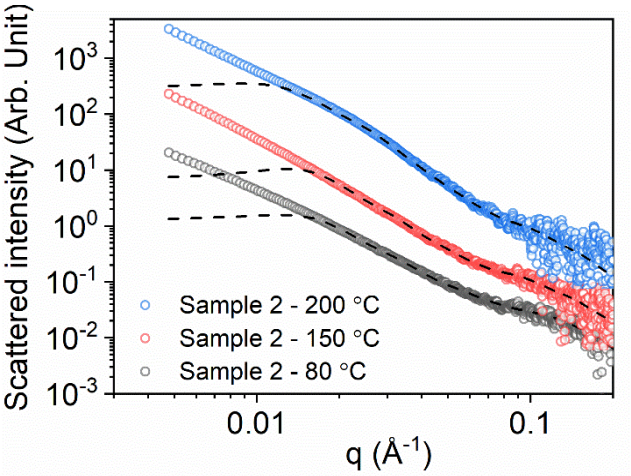

Figure 6. SAXS patterns (dots) and the resulting IRENA fit (dashed line) of PEEL solution containing Au-Cu alloy NPs (sample 2) annealed at 80, 150 and 200 °C during 5h. The curves are shifted in Y axis for a better visualization.

maintained constant during 5 h to ensure a complete coalescence of the NPs at the desired temperature [67].

3.4 UV-Vis spectrophotometry of the annealed NPs

First, a direct naked eyes observation of the solutions upon annealing is made (Figure 4 - inset). No change in colour is observed until a temperature of 150 °C is reached. When reaching 200 °C, the solution turns yellow. Moreover, sedimentation of NPs appears. This points out that aggregation and subsequent growth of the NPs occur during the heating. UV-Vis spectra were recorded for the PEEL solutions containing the NPs. The latter are diluted, after annealing, with ethanol for the different annealing temperatures tested (Figure 4). No change is observed below 90 °C. For an annealing temperature of 150 °C, the absorbance spectra exhibit two peaks, one located at 430 nm and the other at 670 nm. The plasmon resonance at 670 nm can be attributed to the presence of Au-Cu alloy NPs [68] while the one at 430 nm to copper oxide NPs [51]. Finally, for an annealing temperature of 200 °C, only a broad plasmon resonance peak at ~ 680 nm, previously reported for a annealing temperature of 150 °C and corresponding to Au-Cu alloy, is reported. This observation highlights the presence of Au-Cu NPs larger than 20 Å or the aggregation of NPs smaller than 20 Å into larger clusters for a temperature above 90 °C [69]. To confirm the presence of NPs with a diameter of at least 150 Å or aggregates of small NPs, TEM observation has been carried out.

3.5 TEM of the annealed NPs

TEM observation of the NPs annealed at 200 °C has been performed. After annealing, the shape of NPs corresponds to elongated structures (Figure 5a). The mean size of the NPs as obtained by TEM (Figure 5b) is 75 Å (± 30 Å). A high dispersion of the size can be observed due to the specific shape of the NPs. To get an overview of the population of NPs, high resolution TEM micrographs have been recorded (Figures 5c, e, and g). The shape changes from elongated NPs (Figure 5c) to small ligaments (Figure 5g). During annealing, the coalescence of small NPs is observed. Due to the observation of multiple domains within the same NPs (Figure 5c, e, and g), the Ostwald ripening process can be ruled out as the main phenomenon responsible for the growth of the NP [70]. Moreover, the LaMer model cannot be applied in our case [71]. The coalescence of NPs follows two main phases: i) first, the diffusion of the NPs with the creation of a neck between two NPs, and, ii) the disappearance of this neck followed by the surface driven self-diffusion which ultimately leads to one NPs [67]. The reshaping of the NPs during annealing is linked to the temperature and to the surrounding media. By stabilizing some facets of the NPs, the surrounding media can induce preferential growth of NPs [72]. Moreover, the temperature at which all the NP are agglomerated into well-defined spherical NPs depends on the chemical composition of the NP [73]. The formation of NPs having different shapes can thus be expected because the co-sputtering method gives a population of NP whose elemental composition may vary for a single deposition condition. In order to support our previous hypothesis, EDS analysis has been performed on these nanostructures. As expected, the EDS analysis reveals a rather large variety of NP composition inside the same solution (Figures 5d, f, and h). Moreover, the presence of a core-shell structure (Figure 5c) at high magnification is observed. Detailed measurements of the interplanar distances originating from the shell observation highlight a lattice spacing of 2.44 Å corresponding to the lattice parameters of cubic Cu_2O (111) plane. Looking further at the EDS data, it appears that the presence of the shell depends on the composition of the alloy NP core. Indeed, when the alloy NPs are made with more than 50 at.% of copper (Figure 5c, and d), a shell composed of copper oxide forms. Moreover, the EDS analysis confirms the creation of Au-Cu alloy NPs, as previously supported by the UV-Vis spectroscopy results.

3.6 SAXS analysis of annealed NPs

The SAXS measurements were carried out on PEEL solutions containing the NPs annealed at different temperatures. SAXS data along with their respective fit are displayed in Figure 6. The fit involves two populations whatever the annealing temperature. The first population is composed of small particles with a mean radius equal to ~ 10 Å and with a R_{HS} equal to 55 Å. The mean size is similar to that measured for the NPs right after deposition. However, the R_{HS} is bigger, indicating aggregation of the small NPs. The second population corresponds to larger NPs, with a mean radius ranging from 60 to 80 Å and with a R_{HS} ~ 190 Å. Nevertheless, the hypothesis of a core shell structure must be

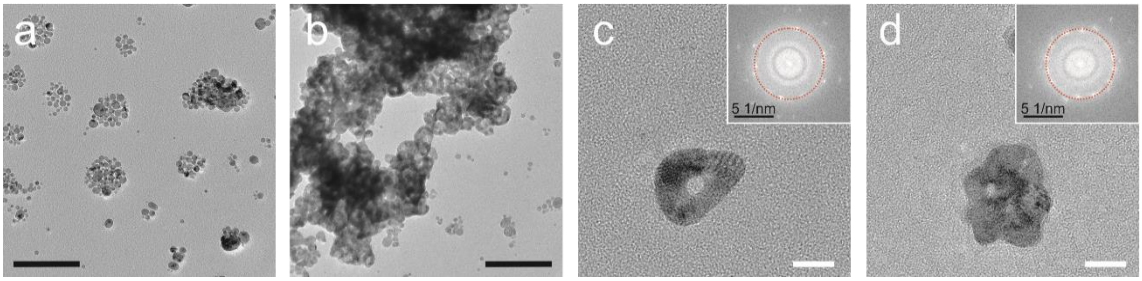

Figure 7. TEM micrographs at (a-b) low and (c-d) high magnifications of Au-Cu alloy NPs (sample 2) annealed at 200 °C during 5 h and dealloyed during 1 min in concentrated nitric acid. Insets correspond to the FFT of the structure display on the figure. Black scale bar: 100 nm, white scale bar: 10 nm.

invoked to fit properly the SAXS data related to this second population. Indeed, as observed on the TEM micrograph (Figure 5) for the sample 2 annealed at 200 °C, some NPs are composed of an alloyed gold-copper core surrounded by a Cu_2O shell. This second population has a bigger mean radius and R_{HS} than the initial NPs. This highlights the increase in the NP size during annealing. The mean NP size calculated from the SAXS data slightly increases, from 68 to 80 Å, as the temperature increases from 80 °C to 200 °C, respectively. The size distribution obtained by TEM analysis on this sample highlight a radius of 75 Å (± 30 Å) while the one reported by SAXS equals 80 Å (± 40 Å). Therefore, the radius achieved for sample 2, which has been annealed at 200 °C, is suitable for the dealloying process and to promote the formation of nanoporous gold NPs.

3.7 Dealloying of the annealed NPs

The dealloying of the NPs is performed by dipping a TEM grid onto which the gold-copper alloy NPs are stuck in concentrated nitric acid during 1 min. The resulting structures have been observed by TEM (Figure 7). Due to the large variety of compositions and sizes of the alloy NPs (Figure 5), it is expected that after such a dealloying process, a wide range of morphologies will be obtained. Indeed, TEM micrographs (Figure 7) reveal a broad panel of architectures from isolated gold NPs and cluster-like structures (Figure 7a) to nanoporous NPs (Figure 7d); even ring-shaped NPs could be observed (Figure 7c).

Two main parameters drive the dealloying of NPs, i.e. their initial size and composition. During dealloying the amount of less noble metal in the alloy (i.e. copper) must be larger than the parting limit (i.e. superior to 40 at.%) [36] otherwise, the more noble metal (i.e. gold) will create a passivation layer which will protect the less noble metal from further dealloying [15]. Moreover, as previously mentioned, the radius plays an important role in the dealloying of NPs. Indeed, the NPs need to be bigger than 120 Å to induce a porosity by dealloying [18]. Following these statements, hypothesis on the formation of these different architectures can be made.

First, due to the small size (radius < 60 Å) or the low content of copper (< 40 at.%) of some alloy NPs, the creation of a porous structure by dealloying will not proceed [18]. This involves the presence of a large amount of solid NPs in our case (Figures 7a). The cluster-like structure observed in Figure 7a is subsequent to the dealloying and can be induced by the drying of the grid. During the drying, the NPs will self-assemble to form disk- or particle- like aggregates [74]. Second, in the case of medium-sized alloy NPs (radius between 60 to 120 Å) having the proper concentration of less noble metal (> 40 at.%), a core−shell structure is observed after electrochemical dealloying [18]. In our case, the free corrosion induces a faster dealloying than the electrochemical dealloying [36]. Hence, the etching of the core, made from the less noble element (i.e. copper) can be expected. This behaviour can explain the creation of the ring-shaped NPs observed (Figures 7b and c). The Fast Fourier Transform (FFT) of the ring-shaped NPs exhibits a d-spacing of 2.31 Å which might indicates the presence of copper residue inside the structure. Finally, for NP characterized by the proper elemental composition (> 40 at.% of copper) and size (radius > 120 Å) porous NPs are obtained after dealloying (Figure 7d). The FFT in inset of Figure 7d reveals a d-spacing of 2.342 Å, very close to the d-spacing of gold (i.e. 2.355 Å), which might point out a low amount of copper in the nanoporous NPs crystalline structure.

Conclusion

In this article, we present an innovative approach to create alloy NPs. Obtaining such alloy NPs is the first step towards the production of nanoporous gold NPs through dealloying, i.e. chemical selective etching, of the copper atoms from the Cu-Au alloy NP. The co-sputtering of gold and copper targets over PEEL liquid leads to the creation of small alloy NPs with a mean radius size of 15 Å which, due to their small size, cannot be used directly for dealloying. In order to overcome this drawback, thermal annealing is performed. After heating the solution containing the NPs during 5h at 200 °C, the gold-copper NPs exhibit a mean radius around 80 Å, which makes them suitable for the dealloying process. After dealloying, a wide range of structures is obtained such as ring-shaped NPs,

close-packed NPs, and nanoporous NPs which are directly linked to the initial composition and size of the alloy NPs. By tuning these parameters, one can accurately control the nanostructures after dealloying. These nanostructures may be used e.g. in future studies to induce a huge enhancement of the heat generation under near-infrared radiation for cancer treatment applications.

Acknowledgements

The authors gratefully acknowledge F. Petitgas (IMN, Nantes) for his technical assistance on the co-sputtering system. This work was supported by the project "Nanomaterials centre for advanced applications", Project No. CZ.02.1.01/0.0/0.0/15_003/0000485, financed by ERDF. A. Fucikova acknowledges the GACR grant number 18-07977Y. S. Konstantinidis and J. Cornil are research fellows of the National Fund for Scientific Research (FNRS, Belgium). S. Konstantinidis and A. Sergievskaya thank the FNRS for the financial support through the "SOLUTIoN" project No T.0134.19. The DFT calculations were supported by the Consortium des Équipements de Calcul Intensif (CÉCI), funded by the Fonds National de la Recherche Scientifique (F. R. S.-FNRS) under Grant No. 2.5020.11.

References

[1] Schmid G 2005 *Nanoparticles* (Weinheim: Wiley-VCH Verlag GmbH & Co. KGaA)

[2] Wender H, Migowski P, Feil A F, Teixeira S R and Dupont J 2013 Sputtering deposition of nanoparticles onto liquid substrates: Recent advances and future trends *Coordination Chemistry Reviews* **257** 2468–83

[3] You J, Zhang G and Li C 2010 Exceptionally High Payload of Doxorubicin in Hollow Gold Nanospheres for Near-Infrared Light-Triggered Drug Release *ACS Nano* **4** 1033–41

[4] Schwartzberg A M, Olson T Y, Talley C E and Zhang J Z 2006 Synthesis, Characterization, and Tunable Optical Properties of Hollow Gold Nanospheres † *The Journal of Physical Chemistry B* **110** 19935–44

[5] Liang H-P, Zhang H-M, Hu J-S, Guo Y-G, Wan L-J and Bai C-L 2004 Pt Hollow Nanospheres: Facile Synthesis and Enhanced Electrocatalysts *Angewandte Chemie International Edition* **43** 1540–3

[6] Xiao J-W, Fan S-X, Wang F, Sun L-D, Zheng X-Y and Yan C-H 2014 Porous Pd nanoparticles with high photothermal conversion efficiency for efficient ablation of cancer cells *Nanoscale* **6** 4345–51

[7] Shen H, You J, Zhang G, Ziemys A, Li Q, Bai L, Deng X, Erm D R, Liu X, Li C and Ferrari M 2012 Cooperative, Nanoparticle-Enabled Thermal Therapy of Breast Cancer *Advanced Healthcare Materials* **1** 84–9

[8] Fan H J, Gösele U and Zacharias M 2007 Formation of Nanotubes and Hollow Nanoparticles Based on Kirkendall and Diffusion Processes: A Review *Small* **3** 1660–71

[9] El Mel A-A, Nakamura R and Bittencourt C 2015 The Kirkendall effect and nanoscience: hollow nanospheres and nanotubes *Beilstein Journal of Nanotechnology* **6** 1348–61

[10] El Mel A-A, Chettab M, Gautron E, Chauvin A, Humbert B, Mevellec J-Y, Delacote C, Thiry D, Stephant N, Ding J, Du K, Choi C-H and Tessier P-Y 2016 Galvanic Replacement Reaction: A Route to Highly Ordered Bimetallic Nanotubes *The Journal of Physical Chemistry C* **120** 17652–9

[11] Preciado-Flores S, Wang D, Wheeler D A, Newhouse R, Hensel J K, Schwartzberg A, Wang L, Zhu J, Barboza-Flores M and Zhang J Z 2011 Highly reproducible synthesis of hollow gold nanospheres with near infrared surface plasmon absorption using PVP as stabilizing agent *J. Mater. Chem.* **21** 2344–50

[12] Tu K N and Gösele U 2005 Hollow nanostructures based on the Kirkendall effect: Design and stability considerations *Applied Physics Letters* **86** 093111

[13] Kosinova A, Wang D, Schaaf P, Kovalenko O, Klinger L and Rabkin E 2016 Fabrication of hollow gold nanoparticles by dewetting, dealloying and coarsening *Acta Materialia* **102** 108–15

[14] Erlebacher J 2004 An Atomistic Description of Dealloying *Journal of The Electrochemical Society* **151** C614

[15] Wittstock A, Biener J, Erlebacher J and Bäumer M 2012 *Nanoporous gold : From an ancient technology to a high-tech material* (Royal Society of Chemistry)

[16] El Mel A-A, Boukli-Hacene F, Molina-Luna L, Bouts N, Chauvin A, Thiry D, Gautron E, Gautier N and Tessier P-Y 2015 Unusual Dealloying Effect in Gold/Copper Alloy Thin Films: The Role of Defects and Column Boundaries in the Formation of Nanoporous Gold *ACS Applied Materials & Interfaces* **7** 2310–21

[17] Wang D and Schaaf P 2012 Nanoporous gold nanoparticles *Journal of Materials Chemistry* **22** 5344

[18] Li X, Chen Q, McCue I, Snyder J, Crozier P, Erlebacher J and Sieradzki K 2014 Dealloying of Noble-Metal Alloy Nanoparticles *Nano Letters* **14** 2569–77

[19] Dupont J and Scholten J D 2010 On the structural and surface properties of transition-metal nanoparticles in ionic liquids *Chemical Society Reviews* **39** 1780

[20] Ishida Y, Udagawa S and Yonezawa T 2016 Growth of sputtered silver nanoparticles on a liquid mercaptan matrix with controlled viscosity and sputter rate *Colloids and Surfaces A: Physicochemical and Engineering Aspects* **498** 106–11

[21] Carette X, Debièvre B, Cornil D, Cornil J, Leclère P, Maes B, Gautier N, Gautron E, El Mel A-A, Raquez J-M and Konstantinidis S 2018 On the Sputtering of Titanium and Silver onto Liquids, Discussing the

Formation of Nanoparticles *The Journal of Physical Chemistry C* **122** 26605–12

[22] Deng L, Nguyen M T and Yonezawa T 2018 Sub-2 nm Single-Crystal Pt Nanoparticles via Sputtering onto a Liquid Polymer *Langmuir* **34** 2876–81

[23] Hatakeyama Y, Morita T, Takahashi S, Onishi K and Nishikawa K 2011 Synthesis of Gold Nanoparticles in Liquid Polyethylene Glycol by Sputter Deposition and Temperature Effects on their Size and Shape *The Journal of Physical Chemistry C* **115** 3279–85

[24] Hatakeyama Y, Takahashi S and Nishikawa K 2010 Can Temperature Control the Size of Au Nanoparticles Prepared in Ionic Liquids by the Sputter Deposition Technique? *The Journal of Physical Chemistry C* **114** 11098–102

[25] Wender H, de Oliveira L F, Feil A F, Lissner E, Migowski P, Meneghetti M R, Teixeira S R and Dupont J 2010 Synthesis of gold nanoparticles in a biocompatible fluid from sputtering deposition onto castor oil *Chemical Communications* **46** 7019

[26] Kim D, Resasco J, Yu Y, Asiri A M and Yang P 2014 Synergistic geometric and electronic effects for electrochemical reduction of carbon dioxide using gold–copper bimetallic nanoparticles *Nature Communications* **5**

[27] Liu C, Cai X, Wang J, Liu J, Riese A, Chen Z, Sun X and Wang S-D 2016 One-step synthesis of AuPd alloy nanoparticles on graphene as a stable catalyst for ethanol electro-oxidation *International Journal of Hydrogen Energy* **41** 13476–84

[28] Kaito T, Mitsumoto H, Sugawara S, Shinohara K, Uehara H, Ariga H, Takakusagi S, Hatakeyama Y, Nishikawa K and Asakura K 2014 K-Edge X-ray Absorption Fine Structure Analysis of Pt/Au Core–Shell Electrocatalyst: Evidence for Short Pt–Pt Distance *The Journal of Physical Chemistry C* **118** 8481–90

[29] Okazaki K, Kiyama T, Hirahara K, Tanaka N, Kuwabata S and Torimoto T 2008 Single-step synthesis of gold–silver alloy nanoparticles in ionic liquids by a sputter deposition technique *Chem. Commun.* 691–3

[30] Suzuki S, Tomita Y, Kuwabata S and Torimoto T 2015 Synthesis of alloy AuCu nanoparticles with the $L1_0$ structure in an ionic liquid using sputter deposition *Dalton Transactions* **44** 4186–94

[31] Sugioka D, Kameyama T, Kuwabata S, Yamamoto T and Torimoto T 2016 Formation of a Pt-Decorated Au Nanoparticle Monolayer Floating on an Ionic Liquid by the Ionic Liquid/Metal Sputtering Method and Tunable Electrocatalytic Activities of the Resulting Monolayer *ACS Applied Materials & Interfaces* **8** 10874–83

[32] König D, Richter K, Siegel A, Mudring A-V and Ludwig A 2014 High-Throughput Fabrication of Au-Cu Nanoparticle Libraries by Combinatorial Sputtering in Ionic Liquids *Advanced Functional Materials* **24** 2049–56

[33] Nguyen M T, Zhang H, Deng L, Tokunaga T and Yonezawa T 2017 Au/Cu Bimetallic Nanoparticles via Double-Target Sputtering onto a Liquid Polymer *Langmuir* **33** 12389–97

[34] Chau Y R, Nguyen M T, Zhu M, Romier A, Tokunaga T and Yonezawa T 2020 Synthesis of composition-tunable Pd–Cu alloy nanoparticles by double target sputtering *New Journal of Chemistry* **44** 4704–12

[35] Corpuz R D, Ishida Y, Nguyen M T and Yonezawa T 2017 Synthesis of Positively Charged Photoluminescent Bimetallic Au–Ag Nanoclusters by Double-Target Sputtering Method on a Biocompatible Polymer Matrix *Langmuir* **33** 9144–50

[36] Chauvin A, Delacôte C, Molina-Luna L, Duerrschnabel M, Boujtita M, Thiry D, Du K, Ding J, Choi C-H, Tessier P-Y and El Mel A-A 2016 Planar Arrays of Nanoporous Gold Nanowires: When Electrochemical Dealloying Meets Nanopatterning *ACS Applied Materials & Interfaces* **8** 6611–20

[37] Ye G, Zhang Q, Feng C, Ge H and Jiao Z 1996 Structural and electrical properties of a metallic rough-thin-film system deposited on liquid substrates *Physical Review B* **54** 14754–7

[38] Girardot R, Viguier G, Ounsy M and Perez J 2017 *Foxtrot* (Synchrotron SOLEIL)

[39] Artacho E, Anglada E, Diéguez O, Gale J D, García A, Junquera J, Martin R M, Ordejón P, Pruneda J M, Sánchez-Portal D and Soler J M 2008 The SIESTA method; developments and applicability *Journal of Physics: Condensed Matter* **20** 064208

[40] Perdew J P, Burke K and Wang Y 1996 Generalized gradient approximation for the exchange-correlation hole of a many-electron system *Physical Review B* **54** 16533–9

[41] Troullier N and Martins J L 1991 Efficient pseudopotentials for plane-wave calculations *Physical Review B* **43** 1993–2006

[42] Nakagawa K, Narushima T, Udagawa S and Yonezawa T 2013 Preparation of Copper Nanoparticles in Liquid by Matrix Sputtering Process *Journal of Physics: Conference Series* **417** 012038

[43] Wender H, Gonçalves R V, Feil A F, Migowski P, Poletto F S, Pohlmann A R, Dupont J and Teixeira S R 2011 Sputtering onto Liquids: From Thin Films to Nanoparticles *The Journal of Physical Chemistry C* **115** 16362–7

[44] Iimori T, Hatakeyama Y, Nishikawa K, Kato M and Ohta N 2013 Visible photoluminescence of gold nanoparticles prepared by sputter deposition technique in a room-temperature ionic liquid *Chemical Physics Letters* **586** 100–3

[45] Shishino Y, Yonezawa T, Udagawa S, Hase K and Nishihara H 2011 Preparation of Optical Resins Containing Dispersed Gold Nanoparticles by the Matrix Sputtering Method *Angewandte Chemie International Edition* **50** 703–5

[46] Turkevich J, Garton G and Stevenson P C 1954 The color of colloidal gold *Journal of Colloid Science* **9** 26–35

[47] Cottancin E, Celep G, Lermé J, Pellarin M, Huntzinger J R, Vialle J L and Broyer M 2006 Optical Properties of Noble Metal Clusters as a Function of the Size: Comparison between Experiments and a Semi-Quantal Theory *Theoretical Chemistry Accounts* **116** 514–23

[48] Deng L, Nguyen M T, Shi J, Chau Y R, Tokunaga T, Kudo M, Matsumura S, Hashimoto N and Yonezawa T 2020 Highly Correlated Size and Composition of Pt/Au Alloy Nanoparticles via Magnetron Sputtering onto Liquid *Langmuir* **36** 3004–15

[49] Deki S, Akamatsu K, Yano T, Mizuhata M and Kajinami A 1998 Preparation and characterization of copper(I) oxide nanoparticles dispersed in a polymer matrix *Journal of Materials Chemistry* **8** 1865–8

[50] Salavati-Niasari M and Davar F 2009 Synthesis of copper and copper(I) oxide nanoparticles by thermal decomposition of a new precursor *Materials Letters* **63** 441–3

[51] Borgohain K, Murase N and Mahamuni S 2002 Synthesis and properties of Cu2O quantum particles *Journal of Applied Physics* **92** 1292–7

[52] Yin M, Wu C-K, Lou Y, Burda C, Koberstein J T, Zhu Y and O'Brien S 2005 Copper Oxide Nanocrystals *Journal of the American Chemical Society* **127** 9506–11

[53] De Luna M M and Gupta M 2018 Effects of surface tension and viscosity on gold and silver sputtered onto liquid substrates *Applied Physics Letters* **112** 201605

[54] Rueden C T, Schindelin J, Hiner M C, DeZonia B E, Walter A E, Arena E T and Eliceiri K W 2017 ImageJ2: ImageJ for the next generation of scientific image data *BMC Bioinformatics* **18**

[55] Schneider C A, Rasband W S and Eliceiri K W 2012 NIH Image to ImageJ: 25 years of image analysis *Nature Methods* **9** 671–5

[56] Guisbiers G, Mejia-Rosales S, Khanal S, Ruiz-Zepeda F, Whetten R L and José-Yacaman M 2014 Gold–Copper Nano-Alloy, " *Tumbaga* ", in the Era of Nano: Phase Diagram and Segregation *Nano Letters* **14** 6718–26

[57] Ascencio J A, Liu H B, Pal U, Medina A and Wang Z L 2006 Transmission electron microscopy and theoretical analysis of AuCu nanoparticles: Atomic distribution and dynamic behavior *Microscopy Research and Technique* **69** 522–30

[58] Bienert R, Emmerling F and Thünemann A F 2009 The size distribution of "gold standard" nanoparticles *Analytical and Bioanalytical Chemistry* **395** 1651–60

[59] Ilavsky J and Jemian P R 2009 *Irena* : tool suite for modeling and analysis of small-angle scattering *Journal of Applied Crystallography* **42** 347–53

[60] Deschamps A and De Geuser F 2011 On the validity of simple precipitate size measurements by small-angle scattering in metallic systems *Journal of Applied Crystallography* **44** 343–52

[61] Partyka-Jankowska E, Leroch S, Akbarzadeh J, Pabisch S, Wendland M and Peterlik H 2014 SAXS studies on silica nanoparticle aggregation in a humid atmosphere *Journal of Nanoparticle Research* **16**

[62] Pedersen J S 1997 Analysis of small-angle scattering data from colloids and polymer solutions: modeling and least-squares fitting I *Adv. Colloid Interface Sci.* 40

[63] Jensen H, Pedersen J H, J⊘rgensen J E, Pedersen J S, Joensen K D, Iversen S B and S⊘gaard E G 2006 Determination of size distributions in nanosized powders by TEM, XRD, and SAXS *Journal of Experimental Nanoscience* **1** 355–73

[64] Beaucage G, Kammler H K and Pratsinis S E 2004 Particle size distributions from small-angle scattering using global scattering functions *Journal of Applied Crystallography* **37** 523–35

[65] Sumi T, Motono S, Ishida Y, Shirahata N and Yonezawa T 2015 Formation and Optical Properties of Fluorescent Gold Nanoparticles Obtained by Matrix Sputtering Method with Volatile Mercaptan Molecules in the Vacuum Chamber and Consideration of Their Structures *Langmuir* **31** 4323–9

[66] Borchert H, Shevchenko E V, Robert A, Mekis I, Kornowski A, Grübel G and Weller H 2005 Determination of Nanocrystal Sizes: A Comparison of TEM, SAXS, and XRD Studies of Highly Monodisperse $CoPt_3$ Particles *Langmuir* **21** 1931–6

[67] Arcidiacono S, Bieri N R, Poulikakos D and Grigoropoulos C P 2004 On the coalescence of gold nanoparticles *International Journal of Multiphase Flow* **30** 979–94

[68] Henkel A, Jakab A, Brunklaus G and Sönnichsen C 2009 Tuning Plasmonic Properties by Alloying Copper into Gold Nanorods *The Journal of Physical Chemistry C* **113** 2200–4

[69] Yang Y, Matsubara S, Nogami M and Shi J 2007 Controlling the aggregation behavior of gold nanoparticles *Materials Science and Engineering: B* **140** 172–6

[70] Thanh N T K, Maclean N and Mahiddine S 2014 Mechanisms of Nucleation and Growth of Nanoparticles in Solution *Chemical Reviews* **114** 7610–30

[71] Turkevich J, Stevenson P C and Hillier J 1951 A study of the nucleation and growth processes in the synthesis of colloidal gold *Discussions of the Faraday Society* **11** 55

[72] Liu Y, Mills E N and Composto R J 2009 Tuning optical properties of gold nanorods in polymer films through thermal reshaping *Journal of Materials Chemistry* **19** 2704

[73] Karlsson M N A, Deppert K, Karlsson L S, Magnusson M H, Malm J-O and Srinivasan N S 2005 Compaction of agglomerates of aerosol nanoparticles: A compilation of experimental data *Journal of Nanoparticle Research* **7** 43–9

[74] Rabani E, Reichman D R, Geissler P L and Brus L E 2003 Drying-mediated self-assembly of nanoparticles *Nature* **426** 271–4